Journal of the European Ceramic Society 45 (2025) 116837

Contents lists available at ScienceDirect

Journal of the European Ceramic Society

journal homepage: www.elsevier.com/locate/jeurceramsoc

# A comparison of the corrosion behaviour over time in 0.5 M NaCl environment of TiCN spark plasma sintered with and without Si aids

Cristina Ojalvo [a], Ana M.R. Senos [b], Angel L. Ortiz [a], Alexandre C. Bastos [b,*]

[a] Department of Mechanical, Energy and Materials Engineering, University of Extremadura, Badajoz 06006, Spain
[b] Department of Materials and Ceramic Engineering, CICECO – Aveiro Materials Institute, University of Aveiro, Campus Santiago, Aveiro 3810-193, Portugal

ARTICLE INFO

*Keywords:*
TiCN ceramics
Corrosion behaviour
OCP
EIS
Polarisation curves

ABSTRACT

The corrosion behaviour over time in 0.5 M NaCl of TiCN spark plasma sintered at low temperature (1400°C) with 5 vol% Si aids and its reference pure TiCN spark plasma sintered at high temperature (2100°C) were investigated by electrochemical techniques (*i.e.,* open circuit potential, current-potential curves, and electrochemical impedance spectroscopy) and microstructural characterisation (*i.e.,* optical microscopy, scanning electron microscopy, and energy-dispersive X-ray spectroscopy), and compared. It is shown that both TiCN materials are very resistant to corrosion in 0.5 M NaCl. After two months of immersion the surfaces remained pristine, without any signs of attack. Their impedance responses revealed capacitive behaviour and very high impedance at low frequencies. The protective passive films strengthened during anodic polarisation and the samples withstood considerable overpotentials before film rupture. The TiCN material fabricated with Si aids is preferable due to its slightly higher corrosion resistance and much lower sintering temperature.

## 1. Introduction

The development of superhard ceramics (>20 GPa) has been crucial in expanding the available selection of machining and cutting tools used in high-speed operations (*e.g.,* turning, grinding, milling, and drilling) applied in the production of parts for many industries (*e.g.*, aerospace, automotive, die and casting manufacturing, to name but a few [1,2]). In service, these tools must withstand extreme conditions in more or less corrosive environments (*e.g.*, cooling lubricants or marine environments). Traditionally, WC-based hardmetals have been the materials of choice for these industrial applications due to their excellent combination of hardness (~16–21 GPa) and toughness (~10–13 MPa•$m^{0.5}$) [3–6]. More recently, TiCN has emerged as a suitable alternative due to its high melting point, excellent mechanical properties, and high chemical stability [7–10].

Currently there are still few studies that have attempted to densify pure TiCN [8,9,11–13], or TiCN with small proportions of graphite [14], because due to its high refractoriness TiCN requires high sintering temperatures (between 1800°C and 2100°C) even by spark plasma sintering (SPS) or more sophisticated sintering techniques (such as hot-isostatic pressing or high-frequency induction sintering). However, it has been shown that it is possible to significantly reduce the densification temperature (down to 1400°C) if the synthesis of nanometric TiCN powders by a mechanically induced self-propagating reaction is combined with SPS [15].

The most popular strategy for densifying TiCN at mild temperatures is liquid phase sintering with metal aids, which results in TiCN cermets. Although not so well studied as WC-Co cermets [16–21], TiCN has been fully densified by SPS with 5 wt% Ni at 1400°C [22], resulting in cermets with ~16.1 GPa hardness and 5.5 MPa·$m^{1/2}$ toughness. TiCN has also been almost fully densified by conventional sintering with 30 vol% Fe-15Ni at 1450°C, resulting in cermets with ~16.5 GPa hardness [23], and with 30 wt% Fe-Cr and Fe-Cr-Mo at 1450–1500ºC, resulting in cermets with ~12.5–14 GPa hardness and 8.5–9.2 MPa·$m^{1/2}$ toughness [24]. More complex TiCN-based cermets with secondary carbides and metal binders have also been prepared. For example, TiCN-based cermets with WC and $Cr_3C_2$ have been fabricated by conventional sintering with 20 wt% Ni or Ni-Cr at 1445°C, resulting in materials with 91–92.7 HRA hardness and 1261–1747 MPa transverse rupture strength [25]. TiCN-based cermets with WC, $Mo_2C$, NbC, VC, and $Cr_3C_2$ have also been fabricated by conventional sintering with 15 wt% Co-Ni, resulting in materials with ~16.5 GPa hardness and 8.75 MPa·$m^{1/2}$ toughness [26]. TiCN as a coating has been deposited on WC-Co cutting tools by cathode arc evaporation physical vapor deposition and chemical vapor

* Corresponding author.
*E-mail address:* acbastos@ua.pt (A.C. Bastos).

https://doi.org/10.1016/j.jeurceramsoc.2024.116837
Received 19 June 2024; Received in revised form 10 August 2024; Accepted 14 August 2024
Available online 15 August 2024

deposition [27,28], and on steel substrates by magnetron sputtering [29]. However, these TiCN-based cermets and coatings have several drawbacks in corrosive environments. First, electrochemical studies on cermets have shown selective dissolution of the metal binder in aqueous corrosive environments [4,21,25,30]. Secondly, the coatings often have defects (such as pinholes, microcracks, pores, *etc*.) [27,29], especially if deposited on complex-shaped parts, which reduce the corrosion protection (because they act as electrolyte channels exposing the substrate to corrosive attack).

There is thus a great interest in TiCN bulk ceramics densified at low temperatures without metal additives. In this respect, transient liquid phase sintering with Si has recently been used to densify $B_4C$, another ultra-refractory carbide, by SPS at only 1400°C [31,32], making it an alternative to the typical metal binders. Shortly afterwards, TiCN was also fully densified by SPS at 1400°C with 5, 15, and 25 vol% Si [33], resulting in the three cases in fine-grained TiCN composites with TiN, SiC, and $TiSi_2$ as secondary phases. This mild sintering temperature is comparable to those commonly used for sintering cermets, with the advantage that no metal binder remains in the microstructure because Si reacts and disappears during sintering. Among these three TiCN materials, 95TiCN+5Si is preferred to 85TiCN+15Si and 75TiCN+25Si because it is the hardest (~22 GPa) and only slightly less tough.

The corrosion resistance of TiCN cermets has been studied to some extent in different corrosive environments such as 0.2 M and 0.5 M $H_2SO_4$ [25,34,35], 1 M HCl [36,37], 1 M NaOH [37], and ~0.5–0.6 M NaCl [11,30]. In contrast, the electrochemical response of fully dense TiCN has been less explored. Nonetheless, the corrosion resistance of almost fully dense TiCN and fully dense TiCN with graphite SPS-ed at 2100°C has been studied in 0.5 M HCl, $H_2SO_4$, and $HNO_3$ [14]. Studies on the electrochemical behaviour of fully dense TiCN in NaCl solution, which is a typical corrosion environment, are scarce and not comprehensive. For example, there are studies performed on TiCN SPS-ed at 2100°C in ~0.6 M NaCl [8], on TiCN hot-isostatic pressed at 1850°C in ~0.5 M NaCl [11,12], and on TiCN SPS-ed at 1800°C [30] in ~0.6 M NaCl, but none of them analyses the corrosion behaviour over time. This work aims to contribute to fill this gap by investigating and comparing the corrosion behaviour over time in 0.5 M NaCl solution of the novel TiCN SPS-ed at mild temperature with 5 vol% Si aids and its reference pure TiCN SPS-ed at much more demanding temperature.

## 2. Experimental procedure

### 2.1. Materials processing

The raw materials were commercial powders of TiCN ($d_{50}$ ~1.65 μm; Grade TiCN 50/50, Treibacher Industrie AG, Germany) and Si ($d_{50}$ ~3.5 μm; Grade AX 05, Höganäs AB, Sweden), which were combined and wet-ball mixed at ~120 rpm (G90 Jar Mill, Gladstone, UK) in abundant ethanol (200 g/l) for 24 h to obtain 95vol%TiCN+5vol%Si after drying the corresponding solution. The resulting powder mixture and the reference pure TiCN powder were individually loaded into graphite dies (2.5 cm diameter) lined with graphite foils and covered with graphite blankets, and SPS-ed (HP-D-10, FCT Systeme GmbH, Germany) in dynamic vacuum under 75 MPa pressure (applied at 300°C) and 100 °C/min heating. 95TiCN+5Si was SPS-ed at 1400°C for 15 min, conditions that promote the full densification of this and other carbides by transient liquid-phase sintering [31,32], and TiCN was SPS-ed at 2100°C for 30 min, conditions that ensure its full densification by solid-state sintering. The resulting materials were ground and diamond polished to a 0.25 μm finish.

### 2.2. Electrochemical measurements

Corrosion specimens were connected from the back to an insulated copper wire using a PELCO conductive silver paint (Ted Pella Inc, USA), and mounted on cold-curing resin (BUEHLER EpoKwick ™ FC, USA). Insulating tape (3 M electroplating tape 470) was then used to delimit the working area of each sample (varying between 0.03 and 1 $cm^2$, depending on the experiment).

Measurements of open circuit potential (OCP), polarisation curves, and electrochemical impedance spectroscopy (EIS) were done with PGSTAT302N or PGSTAT204 Potentiostats (Autolab Metrohm). Testing was performed in electrochemical cells with a three-electrode arrangement, consisting of the working electrode (resin-mounted sample), a platinum counter electrode, and a saturated calomel electrode (SCE) as reference. The measurements were carried out in 0.5 M NaCl aqueous solution (pH = 5.40; conductivity = 30 mS/cm) inside a Faraday cage, at room temperature. The OCP was monitored during the first hour of immersion. Potentiodynamic polarisation curves were measured afterwards, with a scan rate of 1 mV $s^{-1}$, from near OCP to −2.5 V or +2.5 V (*vs* SCE), for the cathodic and anodic branches, respectively. Other samples were immersed in solution and left corroding freely for two months, while EIS measurements were performed after 1 hour, 1 day, 3 days, 1 week, 2 weeks, 3 weeks, one month, and two months, at open circuit potential, with a 10 mV (rms) sinusoidal perturbation, in the 100 kHz to 1–10 mHz frequency range and seven points per decade with logarithmic distribution. Numerical fitting for the EIS spectra was performed with the ZView software (Scribner Associates, USA). Experiments were done in triplicate.

### 2.3. Microstructural characterization

Materials were characterized microstructurally by X-ray diffractometry (XRD; D8 Advance, Bruker AXS, Germany) using pure CuK$\alpha_1$ incident radiation, scanning electron microscopy (SEM; SU70, Hitachi, Japan; TM4000Plus II) and energy-dispersive X-ray spectroscopy (EDS; Xflash Detector 3001, Röntec GmbH, Germany) at 15 kV, and optical microscopy (Panasonic, WV-CP282; Optem zoom 70x; China).

## 3. Results and discussion

### 3.1. Microstructure of the SPS-ed materials

Fig. 1 shows representative SEM micrographs of the fracture surface of the two SPS-ed materials. It can be seen that none of the two TiCN materials have pores, indicative that they are fully dense. It can also be seen that in both cases the grains are equiaxed and faceted, but that due to the different SPS temperatures used (1400°C for 95TiCN+5Si and 2100°C for pure TiCN) there is a vast difference in the microstructural scales. Thus, while pure TiCN is coarse-grained (Fig. 1A), with grains of some tens of micrometres, 95TiCN+5Si is fine-grained (Fig. 1B), with an average grain size not higher than ~1 μm. Fig. 2 shows their XRD patterns. The peaks in the XRD pattern of pure TiCN are doublets (the first more intense than the second), and the peaks in the XRD pattern of 95TiCN+5Si are asymmetric towards higher angles. Both phenomena, and the fact that the XRD patterns were collected with pure CuK$\alpha_1$ incident radiation, indicate that the two materials are composed mainly by a C-rich TiCN phase plus a minor phase of N-rich TiCN. The XRD pattern of 95TiCN+5Si also exhibits weak additional peaks not ascribable to TiCN, but to β-SiC and $TiSi_2$. The presence of these minor phases is consistent with the expectation of densification occurring in this case by transient liquid-phase sintering, in which molten Si reacts with TiCN to form *in-situ* β-SiC and $TiSi_2$ [33].

### 3.2. Open circuit potential

Fig. 3 presents the corrosion potentials of TiCN and 95TiCN+5Si measured during the first hour of immersion in 0.5 M NaCl. The

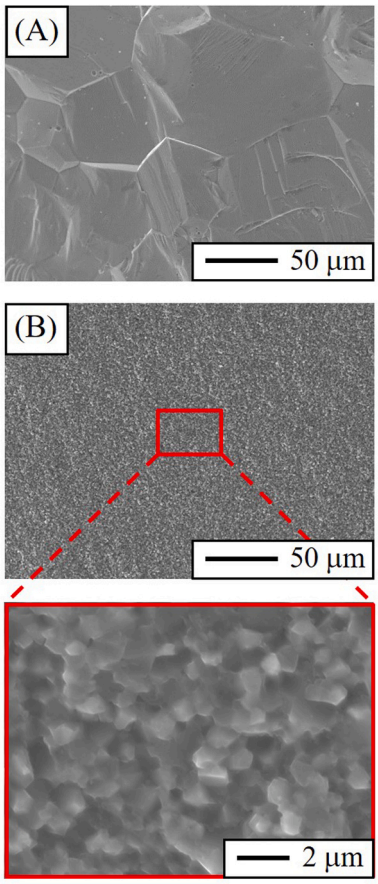


**Fig. 1.** Representative SEM micrographs of the fracture surface of (A) TiCN and (B) 95TiCN+5Si.

potentials fluctuated between 0.042 and –0.093 $V_{SCE}$ for TiCN and between 0.007 and –0.144 $V_{SCE}$ for 95TiCN+5Si, being slightly more positive for the former. In the following days, and during the two months of experiments, both materials showed slight shift towards more positive potentials.

### 3.3. Potentiodynamic polarisation

The anodic polarisation curves of TiCN and 95TiCN+5Si in 0.5 M NaCl are presented in Fig. 4. The currents started very low, in the order of $10^{-8}$ A $cm^{-2}$. Then, as the potential was scanned from OCP to 0.6–0.7 $V_{SCE}$, the current slowly increased until reaching a passive plateau with values around $10^{-6}$ A $cm^{-2}$. After 1.25 $V_{SCE}$ the current increased again in both materials. In 95TiCN+5Si a second passive plateau appeared at 1.5 $V_{SCE}$ with currents around $10^{-4}$ A $cm^{-2}$. In TiCN the current decreased again to the values of the first passive plateau. A final current jump appeared in both materials, at a potential close to 2 $V_{SCE}$ in 95TiCN+5Si and 1.85 $V_{SCE}$ in TiCN. This current jump was accompanied by gas evolution and surface darkening (which started at isolated points on the surface and grew until the surface became completely dark, as seen in the images/videos in the Supplementary Material). SEM micrographs of TiCN and 95TiCN+5Si after the anodic polarisation are presented in Fig. 5. They show a multitude of corroded areas with obvious mass loss, with smaller areas for the material with a finer grain size, *i.e.* 95TiCN+5Si. Fig. 6 shows EDS spectra before and after anodic polarisation confirming that the corroded surfaces of both materials contain oxygen, and therefore the formation of oxide corrosion products.

The behaviour of TiCN during anodic polarisation has been investigated by chemical analyses of the testing solution and Auger spectroscopy of the corroded surface [11,12]. It has been reported that at the beginning the dissolution rate of TiCN is rather low with the formation of $TiO^{2+}$ ions, according to the reaction:

$$2TiCN\,(s) + 6H_2O\,(l) \rightarrow 2TiO^{2+}\,(aq) + 2CO_2\,(g)\uparrow + N_2\,(g)\uparrow + 12H^+\,(aq) + 16e^- \quad (1)$$

A reaction with so many chemical species and electrons hides a complex mechanism behind it. An oxide film was then formed consisting of three layers, the innermost of $TiC_{0.3}N_{0.3}O_{0.4}$, the middle one of TiO, and the outermost of $TiO_2$. This seems to correspond to the first passive plateau observed in this work. The following reactions were proposed:

$$TiCN\,(s) + H_2O\,(l) \rightarrow TiC_xN_yO_z\,(s) + 2H^+\,(aq) + 2e^- \quad (2)$$

$$2TiCN\,(s) + 8H_2O\,(l) \rightarrow 2TiO_2\,(s) + 2CO_2\,(g)\uparrow + N_2\,(g)\uparrow + 16H^+\,(aq) + 16e^- \quad (3)$$

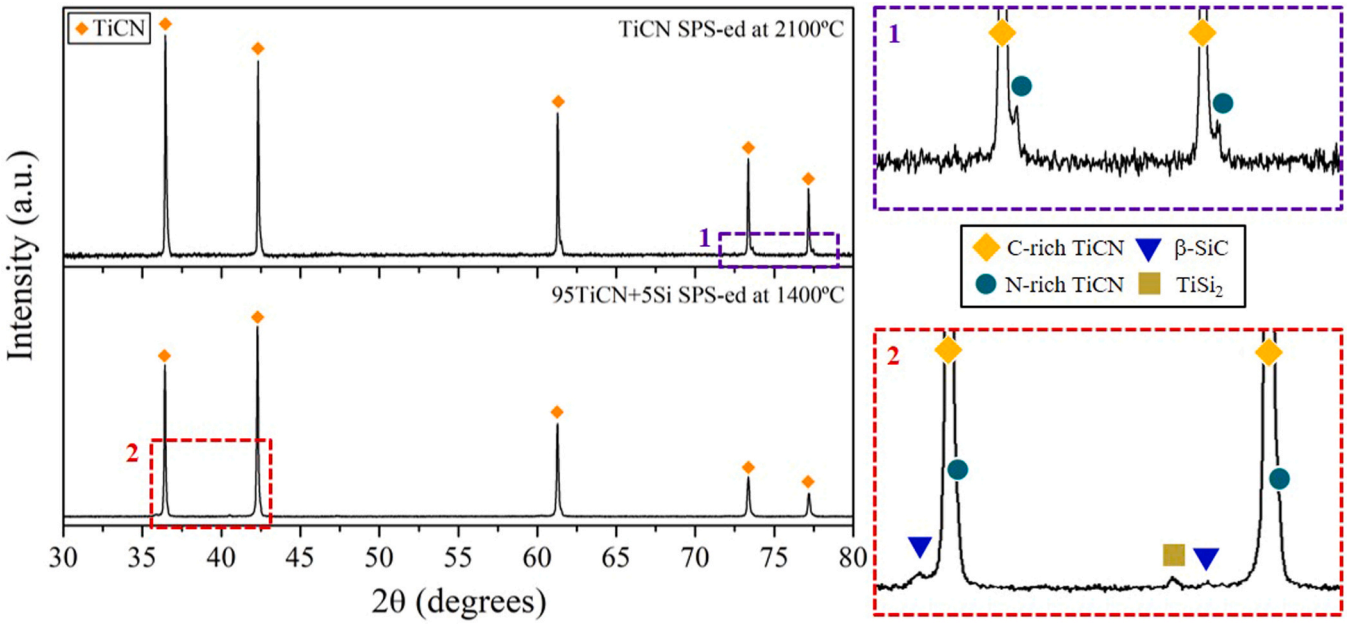


**Fig. 2.** XRD patterns of TiCN and 95TiCN+5Si. The boxes on the right show certain angular intervals in more detail, as indicated.

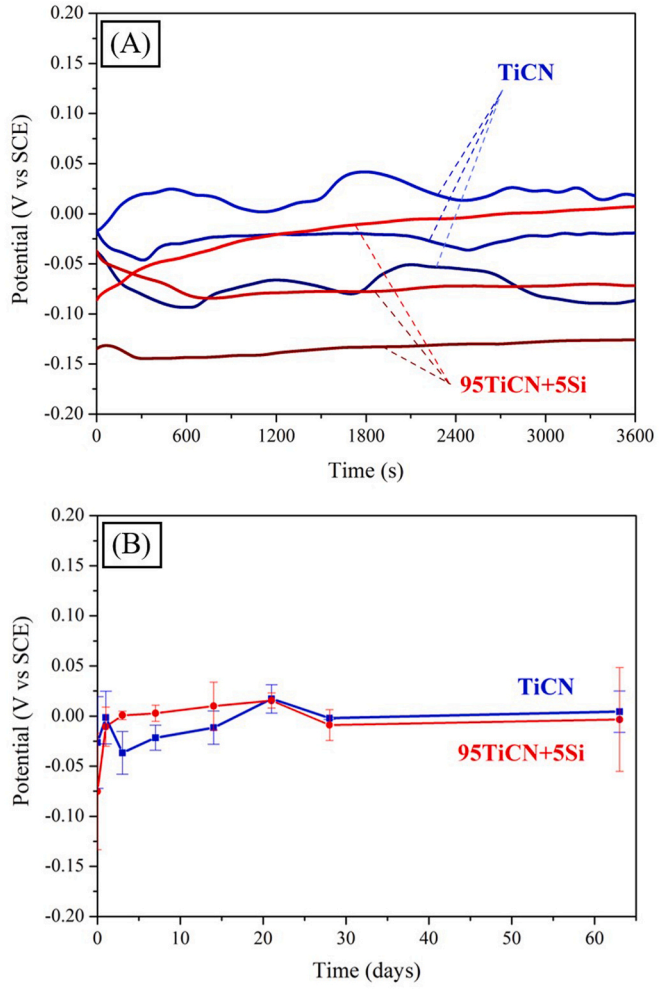


**Fig. 3.** Corrosion potential of TiCN and 95TiCN+5Si measured during (A) the first hour and (B) two months of immersion in 0.5 M NaCl (3 samples of each case).

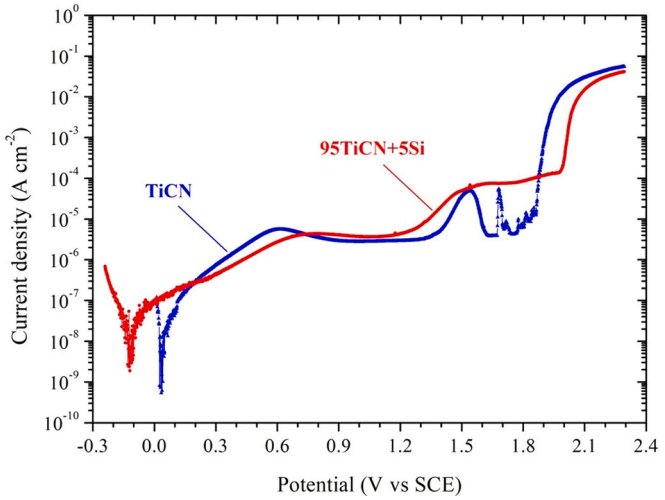


**Fig. 4.** Anodic polarisation curves of TiCN and 95TiCN+5Si in 0.5 M NaCl.

This should also apply to 95TiCN+5Si because it is essentially TiCN, plus the predictable formation of oxides of the minor SiC and $TiSi_2$ phases [38]. EDS analyses made before and after the anodic polarisations support these assumptions.

It has also been reported [11,12] that the surface layer was not protective for potentials >1.8 $V_{SCE}$, and that the specimens dissolved to form tetravalent Ti in solution. A friable film of $TiC_xN_yO_z$ film was formed due to oxygen entering the carbonitride lattice, and the general process is described by Eq. (2).

In this work, the surface attack was accompanied by gas evolution, which started around 2 $V_{SCE}$ and is attributed to water oxidation with oxygen evolution:

$$2H_2O\ (l) \rightarrow 4H^+\ (aq) + O_2\ (g) + 4e^- \quad (4)$$

This reaction occurs at a considerable overpotential, meaning that these surfaces do not easily support electrochemical processes. The passive film was protective up to 1.8 $V_{SCE}$. Reversing the potential scan before the breakdown of the passive film leads to a significant decrease in current, as seen in Fig. 7, which is indicative of the strengthening of the oxide layer.

Fig. 8 compares both fresh and oxidised surfaces with reverse scans. The repetition of the anodic polarisation with oxidised surfaces (after the first polarisation curve has been performed) shows that the oxidised layer has neither protective nor catalytic towards water oxidation. The measured currents are higher in the oxidised surfaces, due to their larger surface area. As shown in Fig. 5, the oxidised surfaces have a micro/nanostructured texture resulting in a higher surface area. The curve shapes were similar on the fresh and oxidised surfaces, except for the absence of the oxidation peak around 1.6 $V_{SCE}$ on the oxidised TiCN.

Table 1 lists the main electrochemical parameters extracted from the set of anodic polarisation curves. The corrosion current densities are very small, in the order of $10^{-8}$ A $cm^{-2}$, being slightly smaller in 95TiCN+5Si. Higher values ($7.37 \pm 3.73 \times 10^{-7}$ A $cm^{-2}$) were found for $TiC_{0.5}N_{0.5}$ fabricated by SPS and immersed in ~0.5 M NaCl [30]. In another work, $TiC_{0.5}N_{0.5}$ fabricated by SPS and immersed in the same solution showed $i_{corr}$ = 11.39 μA and $E_{corr}$ = −0.263 $V_{Ag/AgCl}$ [8]. No previous studies have been found for TiCN SPS-ed with Si.

Anodic polarisation curves are essential in corrosion studies. Cathodic plots are less common, but the information they provide about the kinetics of the reduction reactions occurring at the material surface is also very important. After all, corrosion is the balance between the oxidation of the material and the reduction of chemical species available in the environment. Fig. 9 shows the cathodic polarisation curves of TiCN and 95TiCN+5Si in 0.5 M NaCl. The current measured between the corrosion potential and –0.3 $V_{SCE}$ is the capacitive component of the current with the surface charging as the potential changes. Faradaic processes occur at more negative potentials. The reduction of dissolved $O_2$, as given by the reaction:

$$O_2\ (g) + H_2O\ (l) + 4e^- \rightarrow 4OH^-\ (aq) \quad (5)$$

appears between –0.3 and –1.3 $V_{SCE}$, with a large region of potential under activation control (from –0.3 to –1 $V_{SCE}$) and a small region under diffusion control. Below –1.5 $V_{SCE}$ water reduction occurs with hydrogen evolution:

$$2H_2O\ (l) + 2e^- \rightarrow H_2\ (g) + 2OH^-\ (aq) \quad (6)$$

Reactions (5) and (6) take place at overpotentials higher than the usual which means that these materials do not easily support reduction reactions.

### 3.4. Electrochemical impedance spectroscopy

Further insights about the structure and reactivity of the surfaces were obtained by electrochemical impedance spectroscopy. Fig. 10 shows Bode plots of the impedance response of TiCN and 95TiCN+5Si measured in 0.5 M NaCl for one month. The initial spectra are dominated by the resistive response of the solution at high frequencies, followed by a capacitive response in the remaining frequency range. The impedance was high, around 1 MΩ $cm^2$ at 1 mHz. After 1 day for

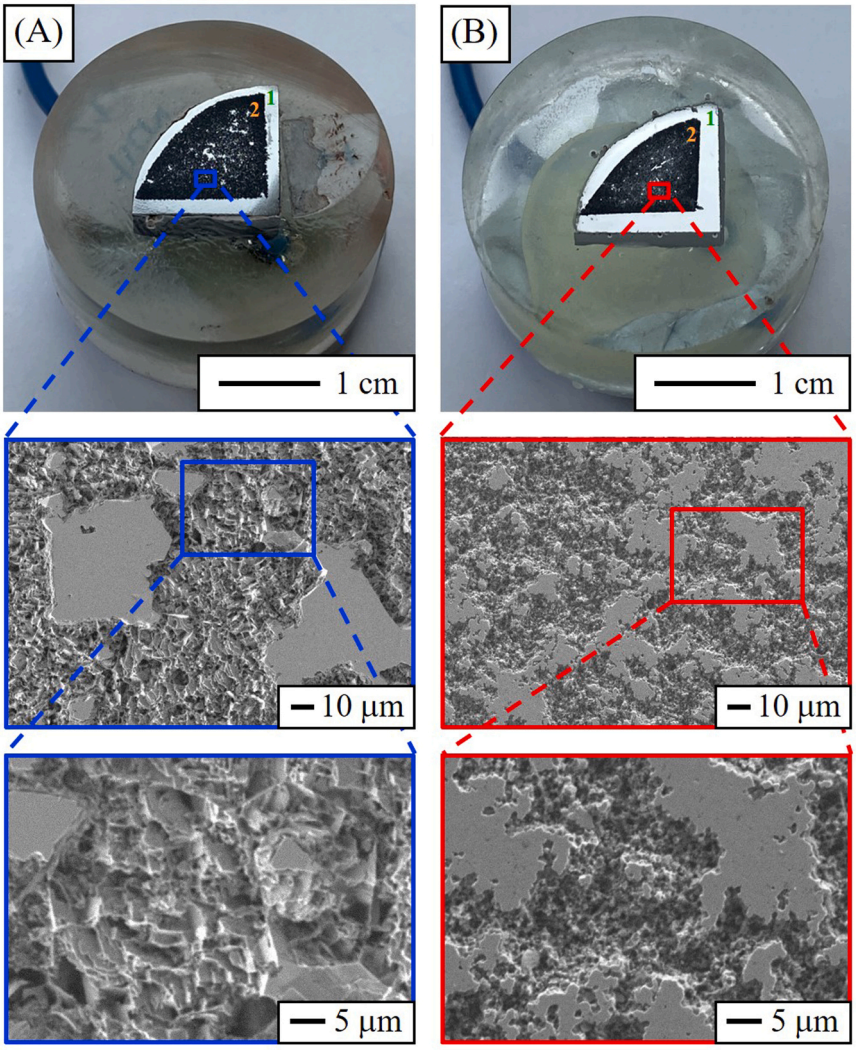


**Fig. 5.** Optical photographs and SEM images of (A) TiCN and (B) 95TiCN+5Si, after anodic polarisation in 0.5 M NaCl.

95TiCN+5Si and 7 days for TiCN a new process appeared at low frequencies with a resistance in the order of $10^4$ Ω $cm^2$ and a capacitance dominating the spectrum at frequencies below 0.1 Hz. Another process was also detected at high frequencies but not well defined. This set of responses was maintained during the 28-day test period (the two-month response is also very similar and is not shown in Fig. 10 for brevity).

Fig. 11 shows the impedance of TiCN and 95TiCN+5Si after 28 days of immersion measured not only at open circuit potential (OCP) but also at OCP±0.5 V, that is, under anodic and cathodic polarisation. This experiment allows identifying the frequency region where the electrochemical process (charge transfer resistance and double layer capacitance) responds. When the samples are polarised from the rest potential (OCP), electrochemical reactions will either be favoured or slowed down. A positive potential shift (anodic overpotential) promotes oxidations and delays or even suppresses reductions, while the opposite occurs during a negative potential shift (cathodic overpotential). Passive elements (like an oxide film) are not affected by the polarization, and so their impedance response does not change. The spectra in Fig. 11 are similar except in the low-frequency region. The spectra show three-time constants associated with three processes, with the respective phase angles maxima centred at 1 kHz, 2–4 Hz, and 5 mHz. Only the process responding in the low frequency region was affected by the polarisation. Therefore, it can be clearly assigned to the electrochemical process taking place on the TiCN or 95TiCN+5Si surfaces. The impedance decrease in the low-frequency region reflects the facilitation of the electrochemical reactions (1) or (2) at OCP+0.5 V and reaction (5) at OCP–0.5 V.

Another series of EIS experiments was performed after subjecting the samples to the polarisation curves. In Fig. 12, OCP corresponds to the spectra obtained on fresh surfaces before polarisation. The potential values in the legend indicate the final potential of the anodic potential scan before the impedance measurement. The spectra at OCP were the same as the spectra after 1 hour immersion shown in Fig. 10. After polarisation the curves shifted to the right, and the capacitances significantly decreased in magnitude. The capacitance $C$ of a film is given by:

$$C = \frac{\varepsilon\, \varepsilon_0\, A}{l} \tag{7}$$

where $\varepsilon$ is the dielectric constant of the film material, $\varepsilon_0$ is the vacuum permittivity, $A$ is the area of the sample, and $l$ is the film thickness. The capacitance decreases after an increase of $l$ or a decrease of $\varepsilon$. Here, the most likely reason for the decrease in capacitance is the increase in the film thickness during the anodic polarisation. Alternatively, the dielectric constant $\varepsilon$ could have decreased due to a chemical transformation of the oxide film during polarisation leading to a new denser and more compact phase. In either case, being thicker or more compact, the new film resulting from the anodic polarisation represents a better protective barrier separating the base material and the corrosive environment. This is consistent with the current decrease in the reverse scan observed in

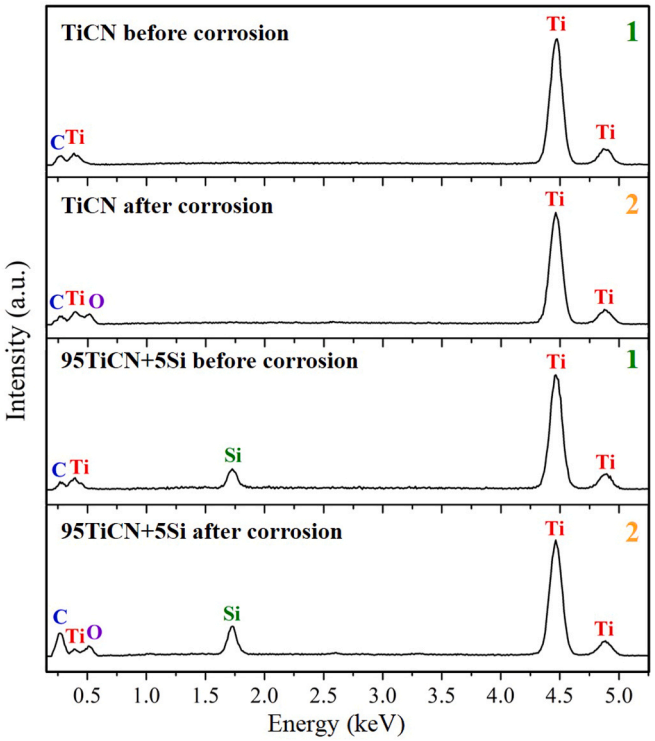


**Fig. 6.** EDS spectra taken at the locations indicated with numbers in Fig. 5. Numbers 1 and 2 correspond to the surface before and after anodic polarisation, respectively.

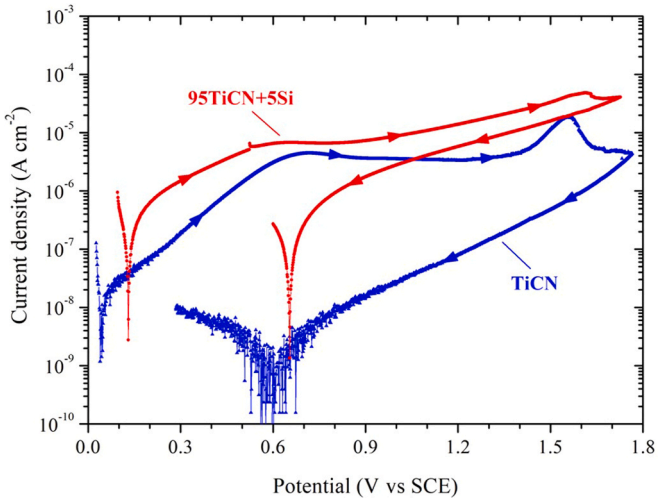


**Fig. 7.** Anodic polarisation curves of TiCN and 95TiCN+5Si in 0.5 M NaCl reversing the scan at 1.7 $V_{SCE}$ (while in the passive plateau).

Fig. 7. A thicker or denser film formed in the forward scan becomes a higher resistance for the current in the reverse scan. The impedance of the surfaces at the first passive plateau (1.6–1.7 $V_{SCE}$), and the impedance measured on surfaces polarised until just before the onset of surface oxidation with gas evolution (2–2.1 $V_{SCE}$) do not differ substantially. Conversely, a significant change was observed in the capacitive response of fully oxidised surfaces, which shifted to the left in the Bode plots. As Fig. 5 shows, the oxidised surfaces are rougher, with a significant increase in surface area. As a result, the capacitances in the two materials increased in magnitude. The ratio of the capacitances on the fresh and oxidised surfaces differed by a factor between 10 and 100. TiCN always showed a higher impedance, with a more capacitive behaviour, while

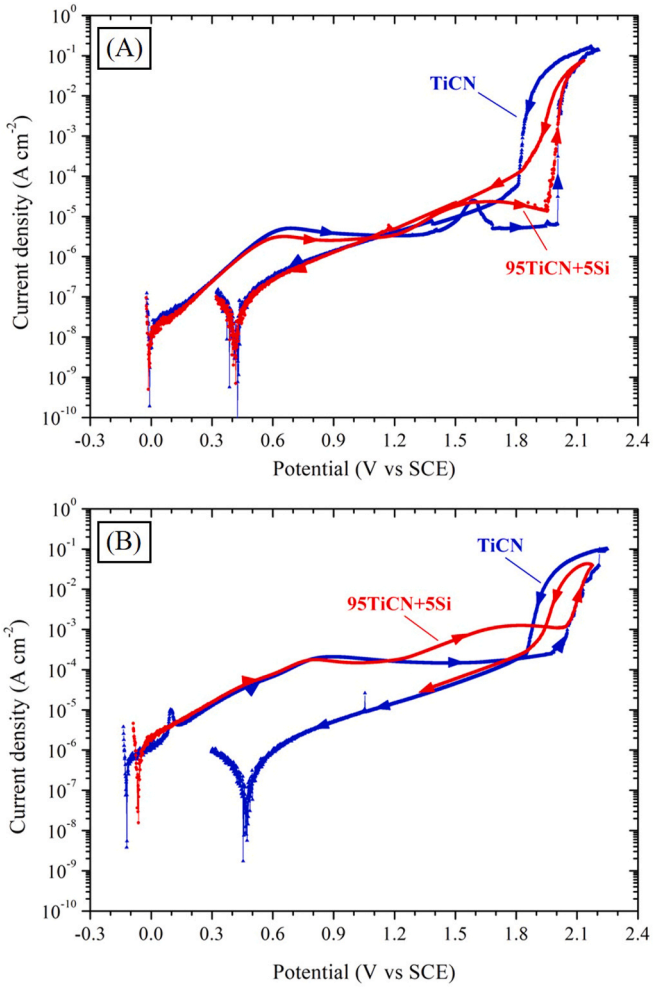


**Fig. 8.** Polarisation curves with reverse scan of (A) fresh surfaces and (B) oxidised surfaces (after previous polarisation until gas evolution) of TiCN and 95TiCN+5Si in 0.5 M NaCl.

the charge transfer was lower in 95TiCN+5Si.

The information gathered from the various impedance experiments can be used to propose tentative equivalent electric circuits capable of explaining the measured responses. The circuits are shown in Fig. 13. The response measured at the beginning of immersion can be explained by the solution resistance ($R_s$) in series with the double-layer capacitance ($C_{dl}$) in circuit A or the passive film capacitance ($C_{pf}$) in circuit B. The capacitances are in parallel with the charge transfer resistance ($R_{ct}$) in circuit A or the passive film resistance ($R_{pf}$) in circuit B. The resistances are so high at the beginning that they are not actually measured (which is why they are drawn with dashed lines). There is always a double layer at the interface of the passive oxide film with the electrolyte solution, $C_{dl}$ being in series with $C_{pf}$. The effective capacitance of two capacitances in series is dominated by the smallest one. The choice between circuit A and circuit B is not easy, but the latter is preferred because the passive film is real. Moreover, it helps to interpret the evolution of the impedance response. The process that appears at lower frequencies (~5 mHz) after a few days of immersion corresponds to the corrosion of the material, which occurs in defects and pores of the passive film. The time constant at higher frequencies (~1 kHz) is attributed to the partial dissolution of the oxide film. Circuit C is used to describe the complete set of responses measured for these samples.

The circuits in Fig. 13 were used to numerically fit the impedance spectra using the Zview program. The results are listed in Tables 2 and 3. In the fitting procedure the capacitances were replaced by constant

**Table 1**
Electrochemical parameters taken from the polarisation curves [a].

| | $E_{corr}$ (V vs SCE) | $i_{corr}$ (A cm$^{-2}$) | $i_{pass}$ (A cm$^{-2}$) | $E_{transp}$ (V vs SCE) |
|---|---|---|---|---|
| TiCN | −0.037 ± 0.032 | 7.2 ± 4.8 ×10$^{-8}$ | 8.2 ± 4.8 ×10$^{-6}$ | 1.87 ± 0.01 |
| 95TiCN+5Si | −0.090 ± 0.041 | 6.2 ± 4.9 ×10$^{-8}$ | 7.4 ± 3.1 ×10$^{-6}$ | 1.94 ± 0.01 |

[a] Mean values and standard deviation from 3 samples of each type.

phase elements (CPE) to account for their non-ideal behaviour [39]. The impedance of a CPE is given by:

$$Z_{CPE} = \frac{1}{Y_0\,(j\,\omega)^n} \tag{8}$$

where $Y_0$ is the frequency-independent admittance, $n$ is the power of the CPE, $j = \sqrt{-1}$ and ω is the angular frequency (in radians). When $n$=1, Eq. (8) becomes the impedance equation of a capacitor. The CPE values were converted to capacitances using the Brug equation [40,41]:

$$C = \sqrt[n]{Y_0}\left(\frac{1}{R_1} + \frac{1}{R_2}\right)^{\frac{n-1}{n}} \tag{9}$$

where $R_1$ and $R_2$ are the resistances in series and in parallel with the CPE, respectively. The values of the fitted parameters in Tables 2 and 3 do not change substantially during the two-month test period, which is a clear indication of the stability of TiCN and 95TiCN+5Si in a NaCl environment. The capacitances of the passive film varied between 3 and 9 μF cm$^{-2}$, and the capacitances of the double layer between 20 and 70 μF cm$^{-2}$. More importantly, the charge transfer resistance, which is inversely proportional to the corrosion rate, was so high that it was not measured. The differences between the two materials are not significant, confirming the high corrosion resistance in aqueous NaCl solution of both TiCN and 95TiCN+5Si. Indeed, all results in this work show that the corrosion resistance of the two materials in 0.5 M NaCl solution is exceptionally high. Therefore, these ceramics can be applied as high-performance materials in marine environments.

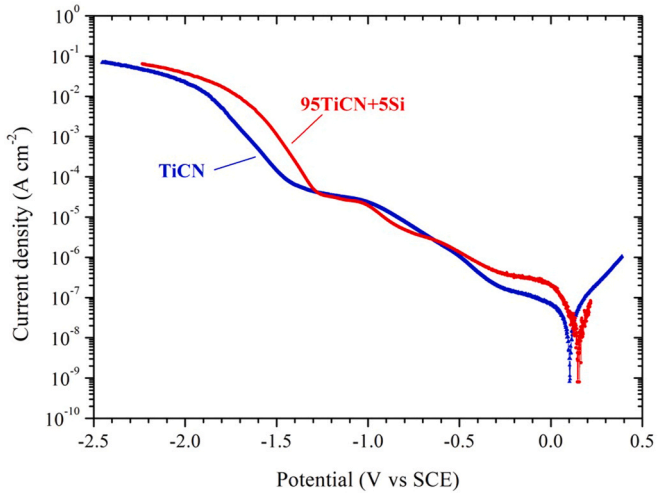


**Fig. 9.** Cathodic polarisation curves of TiCN and 95TiCN+5Si in 0.5 M NaCl.

## 4. Conclusions

The corrosion behaviour over time in 0.5 M NaCl aqueous solution of TiCN and 95TiCN+5Si was investigated using electrochemical methods and microstructural characterisation, and compared. Based on the experimental results and analyses, the following conclusions can be drawn:

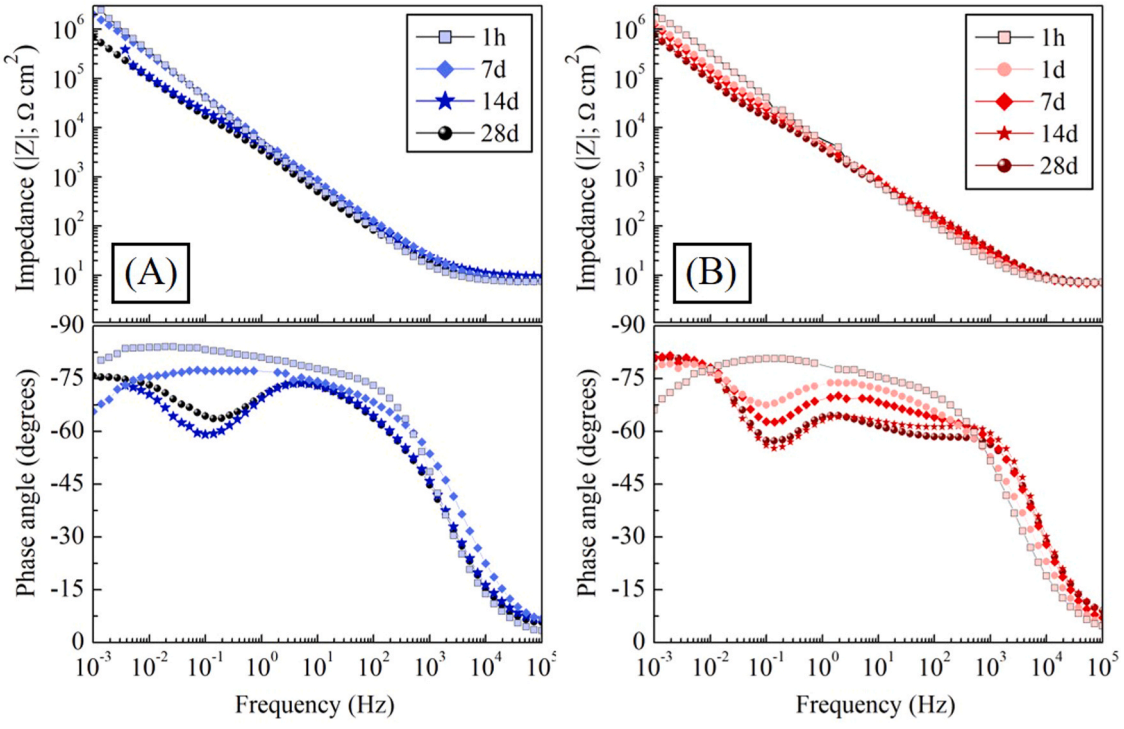


**Fig. 10.** Impedance response of (A) TiCN and (B) 95TiCN+5Si in 0.5 M NaCl.

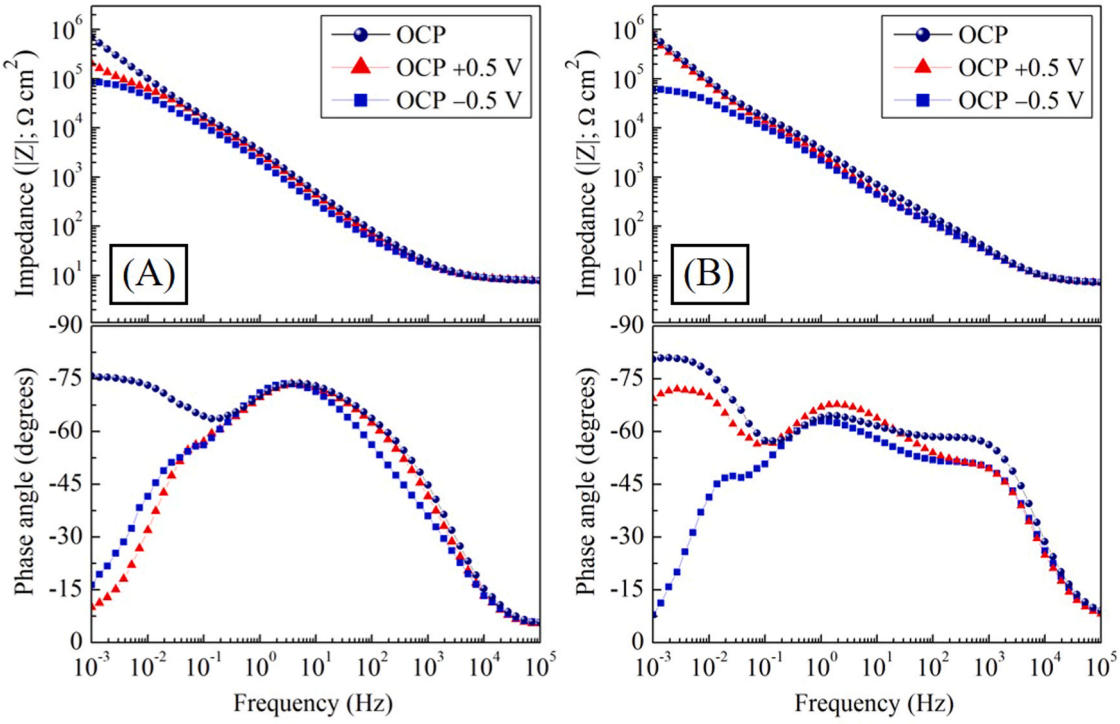


**Fig. 11.** Impedance response of (A) TiCN and (B) 95TiCN+5Si after 28 days of immersion in 0.5 M NaCl, measured at OCP and under anodic and cathodic 0.5 V polarisation.

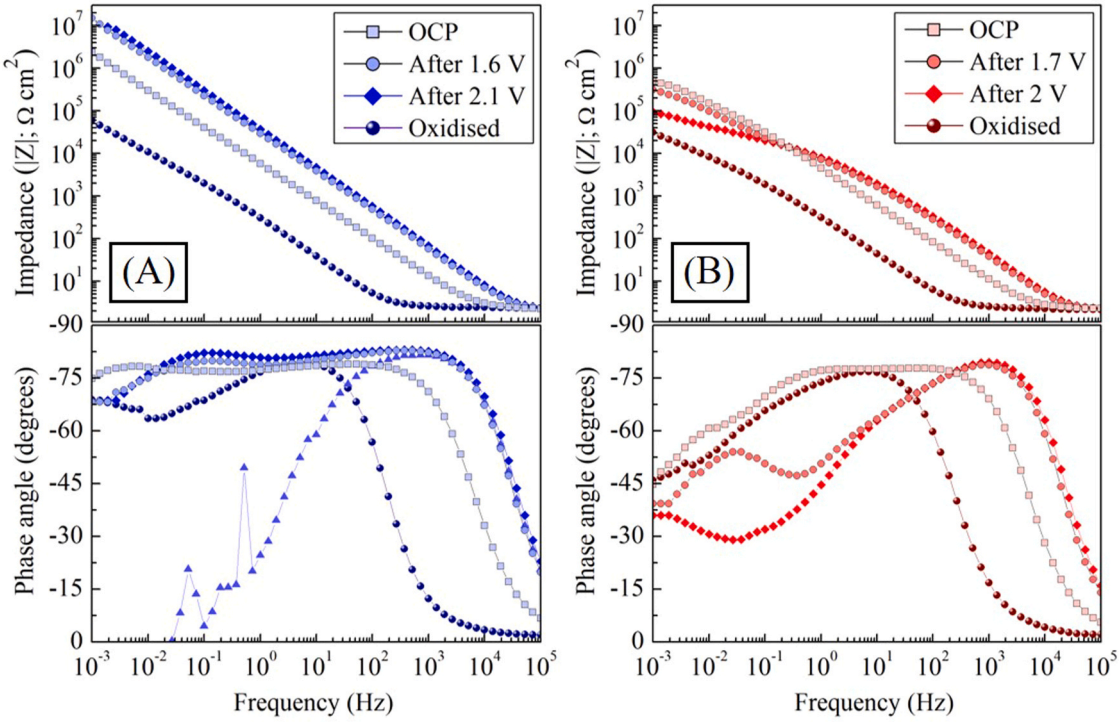


**Fig. 12.** Impedance response of (A) TiCN and (B) 95TiCN+5Si after different polarisation stages.

1. Anodic polarisation curves and electrochemical impedance spectroscopy measurements confirmed the formation of a protective passive film up to about 1.8 $V_{SCE}$ for TiCN and 2 $V_{SCE}$ for 95TiCN+5Si. For higher potentials, the film breaks up and gas evolution occurs. The presence of such a protective oxide film was also confirmed by EDS spectra.
2. Equivalent circuits are proposed for explaining the impedance of TiCN and 95TiCN+5Si. At the beginning of immersion, the response is simply that of the resistance of the solution in series with the capacitance of the passive film. Later, two new time constants appear in the spectra, one at lower frequencies attributed to the electrochemical process (corrosion) occurring at the bottom of the pores

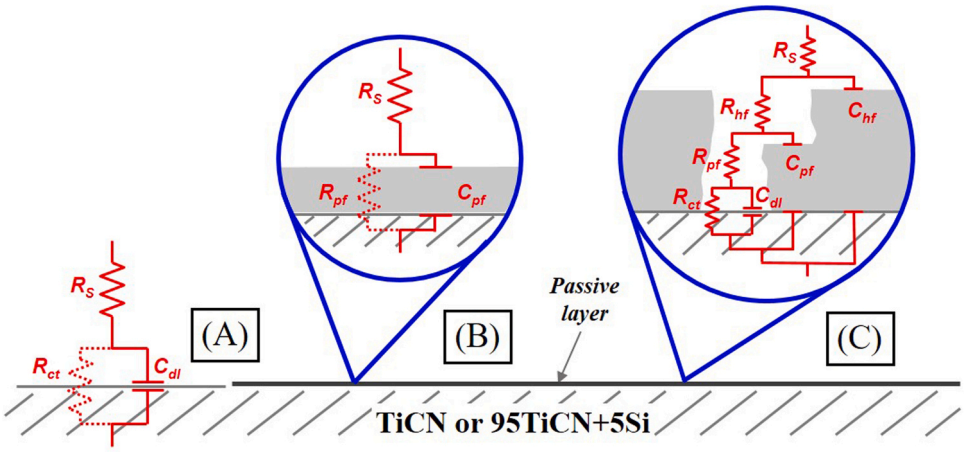


**Fig. 13.** Equivalent circuits used in this work. A – active surface, B – passive surface, C – passive surface with localised corrosion.

**Table 2**
Fit parameters of the impedance spectra measured in TiCN (Fig. 10A).

| Time | $R_s$ ($\Omega$ cm$^2$) | $C_{HF}$ ($\mu$F cm$^{-2}$) | $R_{HF}$ ($\Omega$ cm$^2$) | $C_{pf}$ ($\mu$F cm$^{-2}$) | $R_{pf}$ ($\Omega$ cm$^2$) | $C_{dl}$ ($\mu$F cm$^{-2}$) | $R_{ct}$ ($\Omega$ cm$^2$) | $\chi^2$ |
|---|---|---|---|---|---|---|---|---|
| 1 h | 7.6 | 12.68 | 662.8 | 5.148 | ND | — | — | 0.0010 |
| 1d | 8.0 | 6.405 | 140.2 | 5.181 | ND | — | — | 0.0030 |
| 3d | 7.5 | 5.324 | 142.5 | 3.367 | ND | — | — | 0.0004 |
| 1w | 9.7 | 6.053 | 115.6 | 4.262 | 42408 | 58.34 | ND | 0.0003 |
| 2w | 7.9 | 5.966 | 285.4 | 4.517 | 47821 | 46.44 | ND | 0.0001 |
| 3w | 8.3 | 7.628 | 106.1 | 4.708 | 42571 | 48.97 | ND | 0.0002 |
| 4w | 8.0 | 8.102 | 100.0 | 5.508 | 38394 | 44.54 | ND | 0.0002 |
| 2 m | 7.0 | 3.976 | 98.18 | 8.949 | 439280 | 27.02 | ND | 0.0008 |

**Table 3**
Fit parameters of the impedance spectra measured in 95TiCN+5Si (Fig. 10B).

| Time | $R_s$ ($\Omega$ cm$^2$) | $C_{HF}$ ($\mu$F cm$^{-2}$) | $R_{HF}$ ($\Omega$ cm$^2$) | $C_{pf}$ ($\mu$F cm$^{-2}$) | $R_{pf}$ ($\Omega$ cm$^2$) | $C_{dl}$ ($\mu$F cm$^{-2}$) | $R_{ct}$ ($\Omega$ cm$^2$) | $\chi^2$ |
|---|---|---|---|---|---|---|---|---|
| 1 h | 7.5 | 6.845 | 82.27 | 3.665 | ND | — | - | 0.0024 |
| 1d | 7.2 | 5.184 | 160.2 | 3.299 | 176710 | 20.30 | ND | 0.0010 |
| 3d | 7.1 | 4.629 | 305.2 | 4.234 | 116650 | 27.39 | ND | 0.0005 |
| 1w | 8.5 | 3.885 | 377.6 | 4.689 | 63958 | 47.33 | ND | 0.0004 |
| 2w | 6.6 | 3.173 | 887 | 6.719 | 38326 | 71.54 | ND | 0.0004 |
| 3w | 7.6 | 3.375 | 1021 | 8.158 | 38096 | 73.52 | ND | 0.0006 |
| 4w | 6.8 | 3.369 | 603.5 | 9.130 | 38590 | 74.08 | ND | 0.0006 |
| 2 m | 7.7 | 3.271 | 406.3 | 1.115 | 104540 | 23.18 | ND | 0.0009 |

and defects of the film, and another one at higher frequencies, due to the partial dissolution of the passive film.

3. The corrosion resistance of both TiCN and 95TiCN+5Si is exceptionally high, with corrosion currents in the order of $10^{-8}$ A cm$^{-2}$. The two materials are very attractive for use in marine environments.
4. 95TiCN+5Si is preferred to TiCN because it is slightly more corrosion resistant and is fabricated at a much lower SPS temperature, being more economic and sustainable.

## CRediT authorship contribution statement

**Angel L. Ortiz:** Writing – review & editing, Supervision, Methodology, Funding acquisition, Formal analysis, Data curation, Conceptualization. **Ana M.R. Senos:** Writing – review & editing, Supervision, Methodology, Funding acquisition, Formal analysis. **Cristina Ojalvo:** Writing – original draft, Methodology, Investigation, Formal analysis, Data curation. **Alexandre Bastos:** Writing – original draft, Supervision, Methodology, Investigation, Funding acquisition, Formal analysis, Data curation, Conceptualization.

## Declaration of Competing Interest

The authors declare that they have no competing financial interests or personal relationships that could have appeared to influence the work reported in this paper.

## Acknowledgements

The authors acknowledge the financial support provided by the Ministerio de Ciencia e Innovation (Gobierno de España) under Grant no. PID2022–137393NB-I00, co-financed with FEDER funds. This work was developed within the scope of the project CICECO-Aveiro Institute of Materials, UIDB/50011/2020, UIDP/50011/2020 & LA/P/0006/2020, financed by national funds through the FCT/MCTES (PIDDAC). Cristina Ojalvo acknowledges support from the Spanish Ministry of Universities through the program “Margarita Salas para la formación de jóvenes doctores”, co-funded by the European Union. A.C. Bastos is funded by Portuguese national funds (OE), through FCT - Fundação para a Ciência e a Tecnologia, I.P., in the scope of the framework contract foreseen in the numbers 4, 5 and 6 of the article 23, of the Decree-Law

57/2016, of August 29, changed by Law 57/2017, of July 19.

## Appendix A. Supporting information

Supplementary data associated with this article can be found in the online version at doi:10.1016/j.jeurceramsoc.2024.116837.

## References


[1] X. Tian, J. Zhao, W. Qin, F. Gong, Y. Wang, H. Pan, Performance of ceramic tools in high-speed cutting iron-based superalloys, Mach. Sci. Technol. 21 (2017) 279–290.
[2] K. Gupta, J.P. Davim, Chapter 1 - Introduction to high-speed machining (HSM). High Speed Machining, Academic Press, 2020, pp. 1–25.
[3] A.R. Boukantar, B. Djerdjare, F. Guiberteau, A.L. Ortiz, Spark plasma sinterability and dry sliding-wear resistance of WC densified with Co, Co+Ni, and Co+Ni+Cr, Int J. Refract Met. Hard Mater. 92 (2020) 105280.
[4] P. Pereira, A.M.F. Rocha, J. Sacramento, F.J. Oliveira, L.F. Malheiros, A.M. R. Senos, A.C. Bastos, Effect of different acidic media on the corrosion behaviour of hardmetals with Ni-based binders, Int J. Refract Met. Hard Mater. 110 (2023) 106019.
[5] S.J. Fudger, T.L. Luckenbaugh, B.C. Hornbuckle, K.A. Darling, Mechanical properties of cemented tungsten carbide with nanocrystalline FeNiZr binder, Int J. Refract Met. Hard Mater. 118 (2024) 106465.
[6] J. Hui, X. Sun, Y. Zhou, W. Dong, Y. Luo, S. Zhu, Effect of WC particle size on microstructure and mechanical properties of WC-10CoCrFeNiAl composites, Adv. Eng. Mater. 25 (2023) 230083.
[7] D.E. Wolfe, C.M. DeSalle, C.J. Ryan, R.E. Slapikas, R.T. Sweny, R.J. Crealese, P. A. Kolonin, S.P. Stepanoff, A. Haque, S. Divilov, H. Eckert, C. Oses, M. Esters, D. W. Brenner, W.G. Fahrenholtz, J.P. Maria, C. Toher, E. Zurek, S. Curtarolo, Influence of processing on the microstructural evolution and multiscale hardness in titanium carbonitrides (TiCN) produced via field assisted sintering technology, Materialia 27 (2023) 101682.
[8] G.N. Mekgwe, S.O. Akinwamide, O.J. Akinribide, P.A. Olubambi, Insight into tribological and corrosion behaviour of binderless TiCxNy ceramic composites processed via pulsed electric current sintering technique, Ceram. Int. 48 (2022) 24793–24802.
[9] B.M. Moshtaghioun, J.M. Morgado Chávez, F.L. Cumbrera, D. Gómez, García, Titanium carbonitride fabricated by spark plasma sintering: Is it a ceramic model of carbon-induced Friedel-Fleisher strengthening effect? J. Eur. Ceram. Soc. 41 (2021) 6275–6280.
[10] G. Liu, R. Li, T. Yuan, M. Zhang, F. Zeng, Spark plasma sintering of pure TiCN: densification mechanism, grain growth and mechanical properties, Int J. Refract Met. Hard Mater. 66 (2017) 68–75.
[11] V.A. Lavrenko, V.A. Shvets, A.P. Umanskii, A.B. Belykh, V.M. Adeev, V.N. Talash, Electrolytic corrosion of titanium carbonitride composites, Powder Metall. Met. Ceram. 43 (2004) 72–77.
[12] V.A. Lavrenko, A.D. Panasyuk, M. Desmaison-Brut, V.A. Shvets, J. Desmaison, Kinetics and mechanism of electrolytic corrosion of titanium-based ceramics in 3% NaCl solution, J. Eur. Ceram. Soc. 25 (2005) 1813–1818.
[13] W. Kim, C.Y. Suh, K.M. Roh, J.W. Lim, S. Lee, S.L. Du, I.J. Shon, High-frequency induction heated sintering of high-energy ball milled $TiC_{0.5}N_{0.5}$ powders and mechanical properties of the sintered products, Ceram. Int. 39 (2013) 585–591.
[14] G.N. Mekgwe, O.J. Akinribide, S.O. Akinwamide, P.A. Olubambi, Densification and corrosion properties of graphite reinforced binderless $TiC_{70}N_{30}$ ceramic composites, J. Eur. Ceram. Soc. 44 (2024) 6223–6238.
[15] A. Borrell, A. Fernández, R. Torrecillas, J.M. Córdoba, M.A. Avilés, F.J. Gotor, Spark plasma sintering of ultrafine $TiC_xN_{1-x}$ powders synthesized by a mechanically induced self-sustaining reaction, J. Am. Ceram. Soc. 93 (2010) 2252–2256.
[16] Z. Yao, J. Stiglich, T. Sudarshan, WC-Co enjoys proud history and bright future, Met. Powder Rep. 53 (1998) 32–36.
[17] A. Petersson, J. Ågren, Sintering shrinkage of WC-Co materials with different compositions, Int J. Refract Met. Hard Mater. 23 (2005) 258–266.
[18] M.G. Gee, A. Gant, B. Roebuck, Wear mechanisms in abrasion and erosion of WC/Co and related hardmetals, Wear 263 (2007) 137–148.
[19] L. Vilhena, B. Domingues, C. Fernandes, A. Senos, A. Ramalho, Mechanical and tribological characterization of WC-Co and WC-AISI 304 composites by a newly developed equipment, Materials 15 (2022) 1187.
[20] L.M. Vilhena, C.M. Fernandes, J. Sacramento, A.M.R. Senos, A. Ramalho, Sliding wear and friction behaviour of WC-stainless steel and WC–Co composites, Lubr. Sci. 34 (2022) 247–257.
[21] P. Pereira, A.M.F. Rocha, J. Sacramento, F.J. Oliveira, A.M.R. Senos, L. F. Malheiros, A.C. Bastos, Corrosion resistance of WC hardmetals with different Co and Ni-based binders, Int J. Refract Met. Hard Mater. 104 (2022) 105799.
[22] M. Naidoo, O. Johnson, I. Sigalas, M. Herrmann, Influence of tantalum on the microstructure and properties of Ti(C,N)-Ni cermets, Int J. Refract Met. Hard Mater. 42 (2014) 97–102.
[23] M. de Nicolás, H. Besharatloo, J.M. Wheeler, M. de Dios, P. Alvaredo, J.J. Roa, B. Ferrari, L. Llanes, E. Gordo, Influence of the processing route on the properties of Ti(C,N)-Fe15Ni cermets, Int J. Refract Met. Hard Mater. 87 (2020) 105046.
[24] H.S. Maurya, K. Juhani, M. Viljus, F. Sergejev, J. Kübarsepp, Microstructural evolution and mechanical properties of Ti(C,N)–FeCrMo-based green cermets, Ceram. Int. 50 (2024) 8695–8705.
[25] S. Chen, W. Xiong, Z. Yao, G. Zhang, X. Chen, B. Huang, Q. Yang, Corrosion behavior of Ti(C,N)-Ni/Cr cermets in $H_2SO_4$ solution, Int J. Refract Met. Hard Mater. 47 (2014) 139–144.
[26] A. Elgazzar, S.J. Zhou, J.H. Ouyang, Z.J. Peng, J.T. Yao, Z.G. Liu, Y.J. Wang, Y. M. Wang, Effect of $Si_3N_4$ additive on microstructure and mechanical properties of Ti(C,N)-based cermet cutting tools, Materials 17 (2024).
[27] A. A, I. Matei, M. Pencea, D.E. Branzei, G. Trancə, C.E. Ţepeş, E. Sfət, Ciovica, I. A, G.A. Gherghilescu, Stanciu, Corrosion resistance appraisal of TiN, TiCN and TiAlN coatings deposited by CAE-PVD method on WC-Co cutting tools exposed to artificial sea water, Appl. Surf. Sci. 358 (2015) 572–578.
[28] F. Konstantiniuk, M. Schiester, M. Tkadletz, C. Czettl, N. Schalk, Annealing activated substrate element diffusion and its influence on the microstructure and mechanical properties of CVD TiN/TiCN coatings, Surf. Coat. Technol. 488 (2024) 131079.
[29] N. Madaoui, N. Saoula, B. Zaid, D. Saidi, A.S. Ahmed, Structural, mechanical and electrochemical comparison of TiN and TiCN coatings on XC48 steel substrates in NaCl 3.5% water solution, Appl. Surf. Sci. 312 (2014) 134–138.
[30] Z. Memarrashidi, K.P. Plucknett, The effects of C:N ratio on the aqueous corrosion response of TiC and Ti(C,N) cermets with a $Ni_3Al$-based binder, Int J. Refract Met. Hard Mater. 61 (2016) 162–172.
[31] V. Zamora, F.J. Martínez-Vázquez, F. Guiberteau, A.L. Ortiz, Spark-plasma sintering of boron carbide–silicon carbide composites at 1400 °C from $B_4C$+Si: densification and sintering/reaction mechanisms, J. Eur. Ceram. Soc. 42 (2022) 6876–6888.
[32] V. Zamora, F.J. Martínez-Vázquez, F. Guiberteau, A.L. Ortiz, Unlubricated sliding wear of $B_4C$ composites spark-plasma sintered with Si aids and of their reference $B_4C$ monoliths, J. Eur. Ceram. Soc. 43 (2023) 814–823.
[33] C. Ojalvo, R. Mineiro, C.M. Fernandes, A.M.R. Senos, A.L. Ortiz, Transient liquid-phase assisted low-temperature spark plasma sintering of TiCN with Si aids, J. Eur. Ceram. Soc. 44 (2024) 1511–1519.
[34] B.V. Manoj Kumar, R. Balasubramaniam, B. Basu, Electrochemical behavior of TiCN-Ni-based cermets, J. Am. Ceram. Soc. 90 (2007) 205–210.
[35] B. Allabergenov, O. Tursunkulov, A. Abidov, S.W. Jeong, S. Kim, Mechanical properties of stainless steel composites with titanium carbonitride consolidated by spark plasma sintering, J. Compos Mater. (2016) 1567–1572.
[36] L. Zhao, N. Lin, Y. He, Improvement in microstructure and properties of Ti(C,N)-based cermets with Ruthenium additions, Ceram. Int. 44 (2018) 17553–17561.
[37] L.W. Xu, N. Lin, L.B. Zhao, C. Ma, Z.Y. Wang, Y.H. He, Effect of Ni contents on mechanical properties and corrosion behavior of Ti(C,N)-WC-$Mo_2C$-(Ni,Co) cermets, Mater. Chem. Phys. 252 (2020) 123253.
[38] N. Biscay, L. Henry, T. Adschiri, M. Yoshimura, C. Aymonier, Behavior of silicon carbide materials under dry to hydrothermal conditions, Nanomaterials 11 (2021) 1351.
[39] M.E. Orazem, B. Tribollet. Electrochemical Impedance Spectroscopy, 2nd Ed., Wiley, 2017.
[40] G. Brug, A.L. van den Eeden, M. Sluyters-Rehbach, J.H. Sluyters, The analysis of electrode impedances complicated by the presence of a constant phase element, J. Electroanal. Chem. Interf. Electrochem. 176 (1984) 275–295.
[41] B. Hirschorn, M.E. Orazem, B. Tribollet, V. Vivier, I. Frateur, M. Musiani, Determination of effective capacitance and film thickness from constant-phase-element parameters, Electrochim. Acta 55 (2010) 6218–6227.